RILEM Technical Letters (2021) 6: 169-187
https://doi.org/10.21809/rilemtechlett.2021.151

Alkali-silica reaction – a multidisciplinary approach

Andreas Leemann[1*], Mahsa Bagheri[2], Barbara Lothenbach[1], Karen Scrivener[2], Solène Barbotin[2], Emmanuelle Boehm-Courjault[2], Guoqing Geng[3,4], Rainer Dähn[3], Zhenguo Shi[1,5], Mahdieh Shakoorioskooie[1,6,7], Michele Griffa[1], Robert Zboray[6], Pietro Lura[1,7], Emil Gallyamov[8], Roozbeh Rezakhani[8,9], Jean-Francois Molinari[8]

[1] Concrete and Asphalt Laboratory, Empa, Swiss Federal Laboratories for Materials Science and Technology, 8600 Dübendorf, Switzerland
[2] Materials Institute, Laboratory of Construction Materials, EPFL, 1015 Lausanne, Switzerland
[3] Laboratory for Waste Management, Paul Scherrer Institute, 5232Villigen PSI, Switzerland
[4] National University of Singapore, Department of Civil & Environmental Engineering, Engineering Drive 2, Singapore 117576
[5] Present address: Global R&D, HeidelbergCement AG, Oberklamweg 2-4, 69181 Leimen, Germany
[6] Center for X-ray Analytics, Empa, Swiss Federal Laboratories for Materials Science and Technology, 8600, Dübendorf, Switzerland
[7] Institute for Building Materials (IfB), ETH Zürich, 8093, Zürich, Switzerland
[8] Civil Engineering Institute, Materials Science and Engineering Institute, EPF Lausanne, Station 18, 1015 Lausanne, Switzerland
[9] Department of Mechanical Engineering and Material Science, Duke University, Durham, NC, USA

Received: 17 November 2021 / Accepted: 13 February 2022 / Published online: 28 March 2022 (first version), 06 April 2022 (corrected**)
**This is a corrected version of the article (Fig. 2 and 3 corrected).

Abstract

In the last four years, a multidisciplinary study involving several research groups in Switzerland tackled a number of unsolved, fundamental issues about the alkali-silica reaction (ASR) in concrete. The covered topics include SiO2 dissolution, the characterization of various ASR products formed at different stages of the reaction in both concrete and synthesis, crack formation and propagation. The encompassed scale ranges from nanometers to meters. Apart from conventional techniques, novel methods for the field of ASR have been used, e.g. combination of scanning electron microscopy with dissolution experiments, combination of focused ion beam with transmission electron microscopy, several synchrotron-based methods, synthesis of ASR products for in-depth characterization, time-lapse X-ray micro-tomography combined with contrast-enhancing measures and numerical models of ASR damage based on realistic crack patterns. Key achievements and findings are the quantification of the effect of aluminum on dissolution of different silicates, the variance in morphology and composition of initial ASR products, the differences and similarities between amorphous ASR products and calcium-silicate-hydrate, the link between temperature and the structure of the crystalline ASR products, the behavior of the crystalline ASR products at varying RH, ASR propagation in 4D and numerical modelling based on realistic crack patterns.

Keywords: Alkali-silica reaction; Dissolution; Microstructure; Crystal structure; Crack propagation

Glossary

ASR: alkali-silica reaction
DVS: dynamic vapor sorption
EDX: energy-dispersive X-ray spectroscopy
EXAFS: extended X-ray absorption fine structure spectroscopy (XAS technique)
FEM: finite-element method
FTIR: Fourier transform infrared spectroscopy
GFEM: generalized finite-element method
HPC: high-performance computing
ICP: inductive coupled plasma
PC: Portland cement
FA: fly ash
LC^3: limestone calcined clay cement
ITZ: interfacial transition zone
3D ROI: three-dimensional region of interest
NMR: nuclear magnetic resonance
RH: relative humidity
RVE: representative volume element
SAED: Selected area electron diffraction
SCM: supplementary cementitious materials
SEM: scanning electron microscopy
STXM: scanning transmission X-ray microscopy
TEM: transmission electron microscopy
TGA: thermogravimetric analysis
XT: X-ray tomography
XANES: X-ray absorption near edge structure (XAS technique)
XAS: X-ray Absorption Spectroscopy
XPS: X-ray photoelectron spectroscopy
XRD: X-ray diffraction
XRF: X-ray fluorescence

* Corresponding author: Andreas Leemann, E-mail: andreas.leemann@empa.ch

1 Introduction

Alkali-silica reaction (ASR) causes cracking and substantial damage in concrete structures worldwide, resulting in significantcosts due to repair or replacement [1-3]. The first step of ASR is the dissolution of amorphous or crystalline SiO_2 present in reactive aggregates by the highly alkaline pore solution of concrete [4-8]. The subsequent formation of ASR products in reactive aggregates leads to the generation of stress eventually leading to cracking [9-13]. Such cracks run from the aggregates into the cement paste, connecting with cracks generated in other aggregates [14-16]. Crack networks disperse into the entire cross-section of concrete components degrading their durability and mechanical properties [17-21]. ASR generally is a slow process leading to damage only after several years or even a few decades. Although ASR is one of the major focal points of concrete research since the first cases were reported in the 1940's [22-23], our knowledge is still not sufficient to understand various aspects of the reaction [24-26]. This includes the understanding about various steps in the mechanisms of the reaction, the characteristics of the reaction products formed and the damage development. As a result, both the prevention of ASR in new structures and the management of existing affected structures are based on purely empirical approaches [27-30]. One limiting factor in ASR research has been the limited scope of past projects, which addressed only one specific aspect of the ASR phenomenology, usually without any cross-fertilization with other studies addressing different aspects, e.g. SiO_2 dissolution, the structure of the ASR products formed and crack networks analysis. As such, the potential benefit of synergistic effects between different aspects and different scales has rarely been explored. An ASR-project funded by the Swiss National Science Foundation (SNF) involving several research groups at three research institutes aimed to overcome these limitations using a multidisciplinary approach. It comprises aspects of ASR from the initiation of the reactions starting with SiO_2 dissolution up to the cracking and its mechanical consequences and is addressed by six interlinked subprojects:

- Subproject I: Aggregate dissolution
- Subproject II: Initially formed ASR products in aggregates
- Subproject III: Atomic structure of ASR products
- Subproject IV: Synthetic ASR products
- Subproject V: ASR products and cracking: a 4D view
- Subproject VI: Numerical modelling of mechanics

Subproject I focuses on SiO_2 dissolution as the first step of ASR. The impact of different ions on SiO_2 dissolution is studied using model systems. Additionally, the contribution of different SCM and different aggregates to the composition of the pore solution and its effect on ASR expansion is investigated. ASR products as the key factor leading to stress generation and cracking is targeted from three sides. In subproject II the formation of ASR products is studied using a novel approach combining FIB with TEM and EDS. This makes it possible to follow product formation from the initial to the post-cracking stage in samples from concrete structures and concrete prism tests. Various synchrotron-based methods in subproject III allow an even more in-depth view on the atomic structure of ASR products of samples from ASR-affected structures, selected TEM lamellas provided by subproject II and ASR products synthesized in subproject IV. The later subproject succeeds to identify the effect of temperature and chemical boundaries on the type of crystalline ASR product formed and provides the base for thermodynamic modelling of ASR. The consequences of ASR product formation manifested by cracking are followed in subproject V by employing XT. The measures taken to enhance contrast of both ASR products and cement paste allow to follow ASR product formation and crack development in a 4D-view. Subproject VI seizes on the findings on ASR products and crack formation by employing analytical and numerical modeling from nanometer-scale up to the dimension of a concrete dam.

In this paper, selected highlights of the different subprojects are presented. In order to optimize readability, each subproject is structured as a discrete unit.

2 Novel methods applied on ASR

A collective set of experimental approaches was used in this project. For reading convenience, novelties of these methods are highlighted as follows. More details in regard to the materials and methods used can be found in the supplementary materials.

An innovative scratch-tracking method is introduced to study mineral dissolution in *subproject I*. This method provides reliable information in cases where i) the targeted aggregates have a complex mineralogy and/or ii) the dissolution test may have side reactions such as precipitation of secondary phases.

To investigate the initial ASR products formed in aggregates before cracking occurs, TEM lamellae are cut perpendicular to adjacent quartz grains with FIB in *subproject II*. Further analysis in the TEM includes STEM, STEM EDS and SAED revealing high-resolving data on chemical composition and the structure of ASR products.

Synchrotron-based micro-XRD and micro-XAS were used in *subproject III* to study the samples both extracted from the field concrete and from laboratory-synthesis. The obtained micro-resolved crystal and chemical information were used to interpret the molecular structure of ASR products of various micro-morphology (e.g. crystalline or amorphous). Tomographic micro-XRD scans of extracted ASR product were also collected under changing RH conditions, enabling an in-situ observation of its moisture-sorption behavior and the consequent structural change.

The synthesis of ASR products in *subproject IV* has allowed the analysis of bulk samples by conventional methods like XRD, TGA, FT-IR and Raman microscopy. In addition, the representativeness of the synthesized products to the ASR products formed in aggregates was confirmed.

The addition of contrast-enhancing agents during concrete production has allowed to segment ASR products, cracks formed in aggregates and cement paste by XT in *subproject V*.

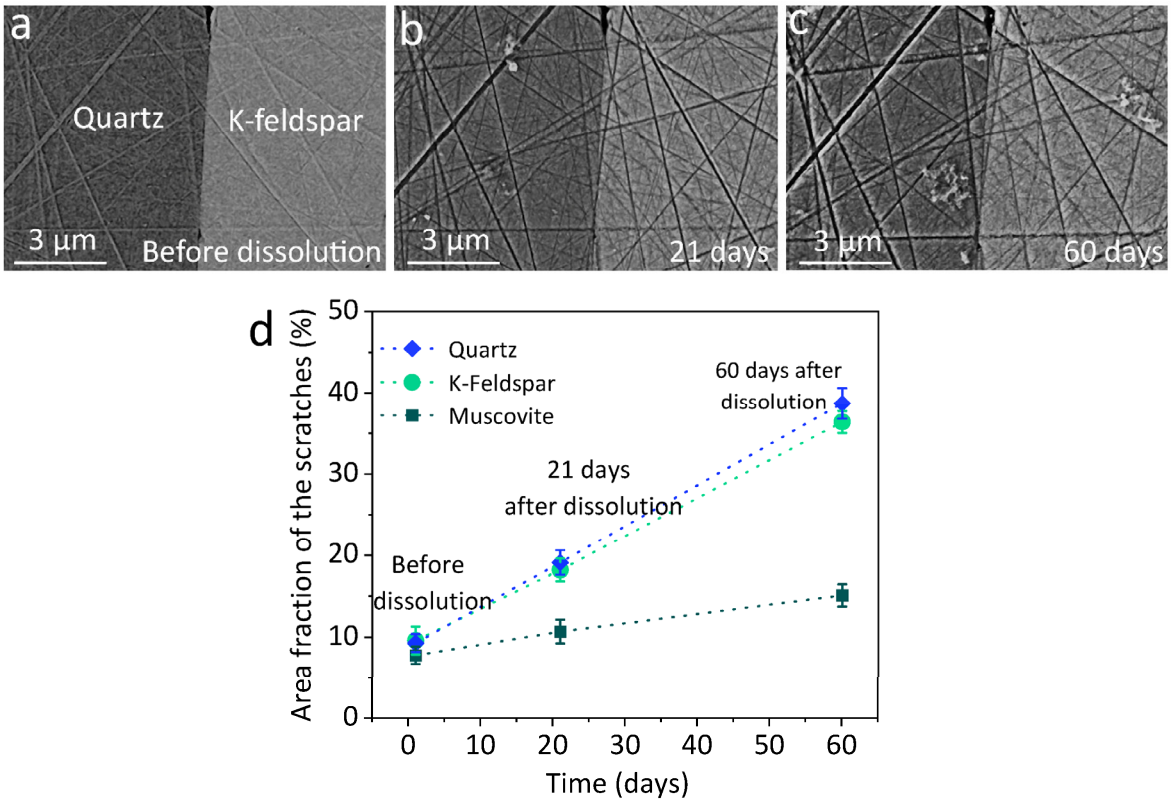

Figure 1. Aligned SEM secondary electron images of (a) quartz and K–feldspar areas of P aggregate before dissolution, (b) after 21 days and (c) 60 days of dissolution in 0.4 M KOH solution at 38 °C, and (d) scratch area fraction (%) for quartz, K-feldspar and muscovite areas of P aggregate before dissolution, after 21 and 60 days of immersion in 0.4 M KOH solution at 38 °C. Adapted from [31].

As such, the applied methodology makes it possible to follow the spatial evolution of ASR at the mesoscale in 4D.

The application of a mesoscale numerical model in *subproject VI* showed that the major part of the macroscopic concrete expansion comes from the cracks growth and opening. Additionally, modelling concrete at the mesoscale by the cohesive element approach provided a well-developed network of thin cracks similar to the tomographic data. The applicability of the computational homogenization multi-scale approach to model ASR-affected macroscopic structures was proven by testing it on laboratory specimens. This model has a unique ability to predict the ASR expansion anisotropy as a function on the applied load based on the crack pattern in the specimen.

3 Subproject I: Aggregate dissolution

3.1 Introduction

Aggregate dissolution, as the first step in ASR [4,25], was studied in subproject I to identify a) which minerals within the aggregates are most reactive and b) how the pore solution composition affects their reactivity.

The dissolution of aggregates was monitored directly by an innovative scratch tracking method, and indirectly by following the increase of Si concentration in an alkaline solution. The scratch tracking method is an image-based method, which tracks the broadening of scratches, created by mechanical polishing, during dissolution [31]. This scratch tracking method enables study of the dissolution of different minerals within an aggregate and is not affected by the precipitation of new phases during the dissolution experiment. In addition, the effect of solution composition on the dissolution rates of amorphous silica, quartz, K-feldspar and Na-feldspar was investigated at high pH values, as observed in cement pore solutions.

3.2 Results

3.2.1 Dissolution of minerals in the aggregates

Figure 1 shows aligned SEM secondary electron images of areas of P aggregate (gneiss/quartzite, see S1.1) containing quartz and K-feldspar (a) before and (b and c) after dissolution in 0.4 M KOH. The width of the scratches increases clearly for both quartz, Na- and K-feldspar with time [31]. The increase of the scratch area with time is quantified in Figure 1d. The scratch-tracking method revealed significant dissolution of quartz, Na-and K-feldspar at high pH values, while micas such as muscovite reacted much more slowly. These observations were confirmed by solution analysis, which showed a clear increase of dissolved Si for all aggregates and of K and Al for the aggregates rich in feldspar as detailed in [31]. These results agree with the reported dissolution rates for quartz and Na-feldspar at pH 12.3 and at 25 °C [32–38], while the dissolution rate of K-feldspar measured at pH 12.7 is slightly lower than reported in literature at the same temperature. The noticeably slower dissolution rate for muscovite at high pH agrees well with other observation [39-41].

3.2.2 Effect of different ions on dissolution of mineral powders

Mainly the pH value and the presence of dissolved aluminum affected the dissolution kinetics strongly under alkaline conditions. While higher pH values increased the dissolution rate of amorphous silica and quartz, aluminum concentrations between 0.1 to 3 mM slowed down the dissolution rate of amorphous silica, quartz, Na- and K-feldspar 4 to 200 times, and the effect was stronger at lower pH values (see Figure 2), in agreement with previous observations [42,43].

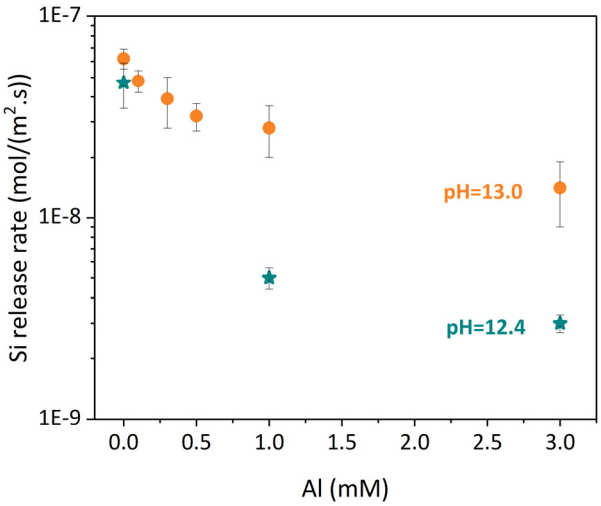

Figure 2. Si release rate (mol/(m^2·s)) from amorphous silica at 40 °C as a function of Al concentration at pH 12.4 and 13. Adapted from [43].

The influence of various elements on the dissolution rates of amorphous silica, quartz and feldspars in alkali solutions is summarized in Figure 3, based both on the increase of Si concentration during dissolution in KOH and based on the scratch-tracking method. Note that in many cases the interpretations of the measured Si concentrations were not possible due to the precipitation of secondary phases such as C-S-H as detailed in [43]. In the presence of Ca or Li, the combination of both methods was important. Following the increase of Si concentrations in solutions with Ca or Li gave misleading results due to precipitation of C-S-H and lithium silicates, which lowered Si concentration resulting in low apparent dissolution rates. In contrast, quantification by the scratch-tracking method showed clearly an increase in dissolution rates of quartz and feldspars in the presence of Ca, Li and possibly sulfate as summarized in Figure 3. The acceleration of quartz and feldspar dissolution might be related to the tendency of Li to form surface complexes [32,44,45]. Lithium salts are known to prevent ASR expansion [46,47]. Based on the observations reported here, this suppression of ASR by Li is not related to any kinetic hindrance of dissolution, but rather due to the change of ASR product. The presence of lithium is reported to lead to an ASR product containing Li but with lower Ca/Si and (Na+K)/Si [48-50].

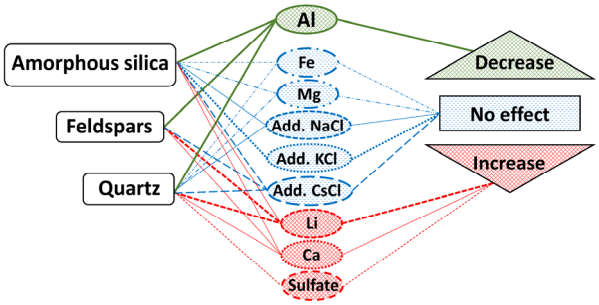

Figure 3. Effect of different ions on the dissolution rate of amorphous silica, quartz and feldspars under alkaline conditions. Adapted from [43].

The presence of iron, magnesium or additional NaCl, KCl or CsCl, had no significant effect on the dissolution. Only Al slowed down the dissolution rate significantly, and the effect of aluminum was stronger at lower pH values [43].

The dissolution experiments allowed studying the effect of ions separately. It clearly identified that alkali hydroxide and thus high pH values as well as calcium are not only needed for the formation of ASR products but also accelerate the dissolution kinetics of SiO_2-containing minerals present within the aggregates. This is in good agreement with the faster expansion due to ASR formation observed at higher pH values [51,52].

3.3 Summary and conclusions

The results show that:

- The dissolution rates of amorphous silica, quartz and feldspar in alkaline solutions are considerably higher than those of micas such as muscovite.
- Increasing pH value increases the dissolution rate of amorphous silica, quartz and feldspar.
- The presence of calcium accelerates the dissolution of amorphous silica, quartz and feldspars, indicating that calcium is not only needed for the formation of ASR products [5,53], but that its presence accelerates the dissolution.
- The presence of lithium accelerates quartz dissolution, indicating that Li suppresses ASR expansion not by slowing down the dissolution, but possibly due to the change of ASR product.

Among all studied ions, only Al could effectively slow down the dissolution of quartz, amorphous silica, Na-feldspar and K-feldspar. The lower dissolution rate was more distinct at pH 12.4 than at pH 13, which could be associated to a higher tendency of Al to sorb on the surface at lower pH values.

The most efficient way to increase Al concentrations and decrease pH values in the pore solutions of cements is the use of Al-rich SCMs such as fly ash and metakaolin. Silica fume is efficient in decreasing pH. The presence of 10-15% of metakaolin can increase Al concentration to 1 to 3 mM [42,50], which decreases the dissolution rates of amorphous silica and quartz by a factor of 10 to 100. However, the alkalinity of the pore solution is still the governing factor of SiO_2 dissolution rate.

4 Subproject II: Initially formed ASR products in aggregates

4.1 Introduction

Detecting ASR in its early growth stage is a key point towards understanding the mechanisms of product formation and further concrete expansion. With the combined use of FIB and TEM techniques [54], the morphology, composition and structure of early-stage ASR products were determined. Concrete from laboratory samples in accelerated conditions (composition given in supplementary materials) and field samples have been analyzed and compared. Analyzed area were located between adjacent quartz grains in the periphery of aggregate particles.

4.2 Results

4.2.1 PC accelerated test and field samples

The following key findings were established:

Morphology

Two morphologies were observed at early stage (Figure 4a), as well as in later age field samples (Figure 4b). Both granular and platy ASR products (Figure 4) were found. An interesting characteristic is that both products morphologies can occur in the same crack. The granular product is located at the aggregate interface, whereas the platy product seems to be present more often in the center of the crack.

Composition

The analyzed products all contain Si, Ca, K and traces of Na in the ratios:

- Ca/Si from 0.3 to 0.5
- [K+Na]/Si from 0.3 to 0.5

Some analyzed areas display a considerably lower Ca/Si or alkali/Si ratio due to the partial inclusion of quartz within the interaction volume of the electron beam. This cannot be prevented due to the low amount of product present and the crack dimensions in the sub-micrometer range.

A slight difference in Ca and K repartition was systematically observed in all the samples (accelerated and field) between the granular and the platy product. The granular product seems to contain more calcium than the platy one (Figure 5a), as also confirmed by the synthetic sample analysis from subproject IV [55]. The difference of composition can also be due to the position of the product in the crack. Close to the aggregate surface, the product tends to contain more calcium, whereas with greater distance to the surface, the product tends to contain more alkali. FIB lamellae analyzed in subproject III using synchrotron-based micro-XRD absorption confirmed the TEM findings in regard to calcium and alkali inhomogeneity in the ASR products [56]. Additionally, in the synthetic sample both a crystalline ASR product K-shlykovite and an amorphous ASR product (ASR-P1) are formed [55], further supporting the occurrence of at least two different phases.

Structure

The diffraction ring formed in the SAED of the platy product indicates a certain degree of crystallinity both in accelerated and field samples (Figure 5b). The granular product shows only a diffuse diffraction ring, indicating its amorphous nature. Again, this is supported by the results obtained in the analysis of these two products in [56] and the similarity to the structure of the synthesized ASR products, that is K-shlykovite and ASR-P1 [55].

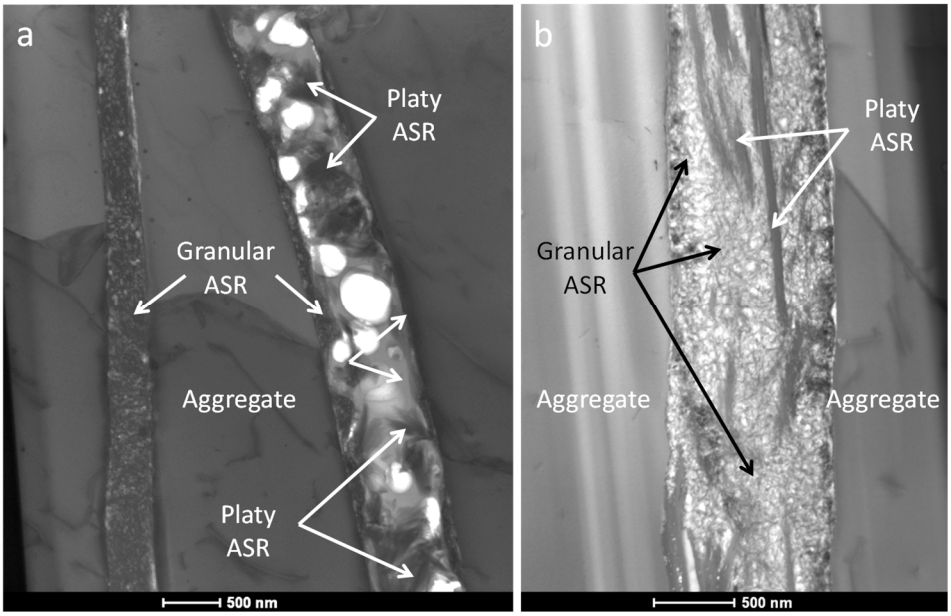

Figure 4. (a) ASR granular and platy product filling cracks in SiO_2 mineral phase after 4 weeks in accelerated conditions and (b) collected in field concrete.

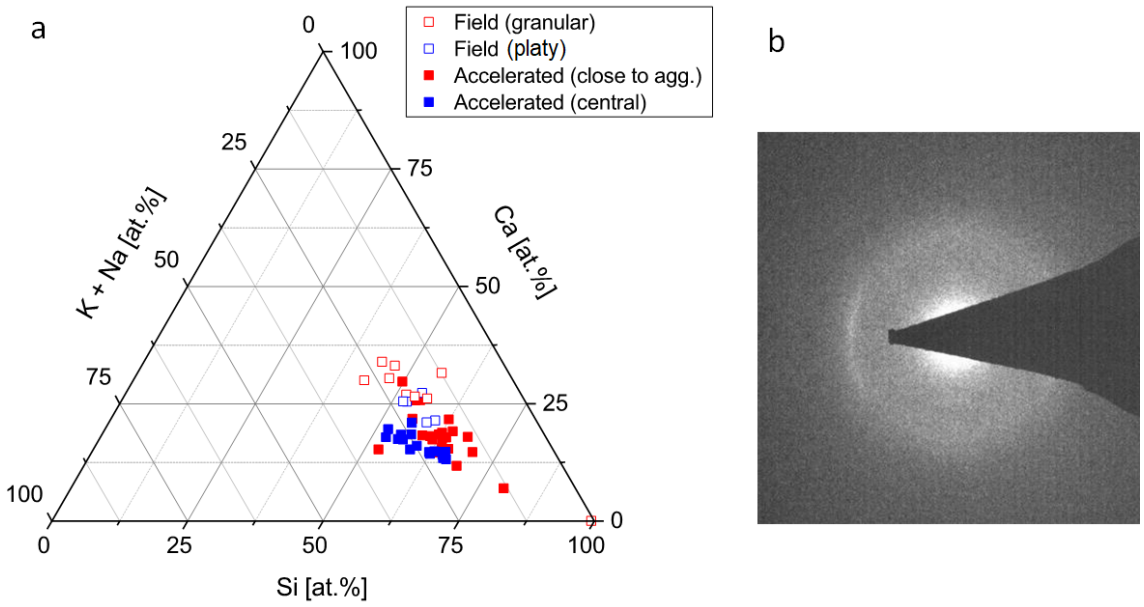

Figure 5. (a) Ternary diagram presenting the ASR products composition in atomic %, normalized among Si, Ca, K and Na. (b) Slightly nanocrystalline behavior of the early-stage platy product in an accelerated laboratory sample as analyzed by SAED.

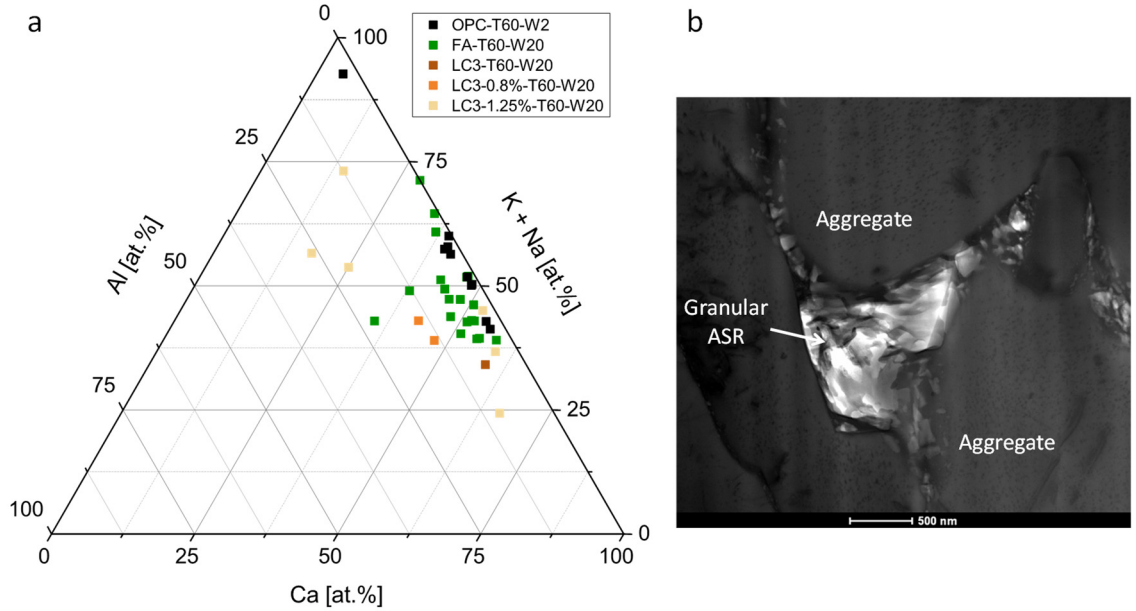

Figure 6. (a) Ternary diagram presenting the ASR products composition present in different concrete mixtures in atomic-%, normalized among Ca, Al, K and Na. (b) Morphology of ASR product in FA containing sample, appearing at grain boundaries.

4.2.2 PC+FA/LC^3 accelerated test samples

After 20 weeks in accelerated conditions in the laboratory at 60 °C and 100 % RH, no expansion was observed, and very little ASR product was found in FA (fly ash) and LC^3 (ternary blends containing PC, metakaolin and limestone) samples. The rare occurrence of ASR product made its analysis difficult, however the composition of some areas like in Figure 6b were analyzed.

Compared with PC samples, the morphology is the same as the granular product (FA sample). In contrast to the PC samples, traces of Al are present. In the ASR product, Al seems to be preferentially located at the interface with the aggregate, indicating an uptake at the aggregate surface rather than in the product. The results are consistent with the previous observations that presence of Al does not affect the morphology and structure of the ASR products [50,57]. This supports the theory that the dissolution rate of silica is reduced by aluminum adsorption at the silica surface [43,58].

4.3 Summary and conclusions

The analysis of ASR products combining FIB with TEM and EDS clearly reveals that different ASR products are formed, displaying a certain variation in chemical composition.

Moreover, there is no clear distinction between amorphous and crystalline ASR products. Both the morphology and the results obtained with SAED indicate that there is continuous transition between the two, from clearly amorphous phases to various nanocrystalline ASR products to the well-crystallized ASR products as described for example in [56,57,59]. At the same time, this transition seems to be the result of a maturation process with the amorphous phase representing the initial product.

5 Subproject III: Atomic structure of ASR products

5.1 Introduction

The subproject III focuses on the microscale crystal-chemical investigation of ASR products from both damaged concrete structures and laboratory synthesis. Using synchrotron-based micro X-ray absorption spectroscopy (micro-XAS) and micro X-ray diffraction (micro-XRD), the chemical environment of K and Ca in the crystalline ASR products were found to be highly consistent, despite the fact that the samples were collected from various structures throughout Europe. Their molecular configurations all resemble the layered-silicate mineral shlykovite ($KCa[Si_4O_9(OH)]\cdot 3H_2O$). More information on shlykovite is presented in section 6.2.1. A 3D tomographic XRD study was done on an ASR product vein while subjecting it to an in-situ wet-dry cycle. Upon wetting, the swelling of the product vein was negligible, although basal-spacing enlargement was observed for some ASR nano-crystals.

Results from subproject III add novel insights to the crystal structure of the nano-crystalline ASR products, and its variation as a function of elemental composition, water content and pressure.

5.2 Results: Atomic structure and property of ASR products

5.2.1 Structural relationship with shlykovite and C-S-H

SEM images have unveiled the micro-morphological variations of ASR products [59,60]. Crystalline and amorphous products are often observed inside and outside the damaged aggregates, respectively. It is however difficult to study their structure, due to the lack of sensitive micro-probes. Here, micro-regions in the field samples were investigated using micro-XAS. Their Ca *K*-edge XAS are plotted in Figure 7a. The spectra of the crystalline ASR products are observed to be highly comparable. The spectra of the amorphous regions are also almost identical. This indicates that the ASR products from different sources share highly comparable molecular structure. Meanwhile, the spectra of the crystalline and amorphous ASR are clearly different from each other, with a shift of 0.3-0.6 eV for most absorption peaks. The minor peaks C' and D in the crystalline phases are also not observed in the amorphous phases, suggesting a substantial difference of the chemical environment between the crystalline and amorphous phases.

Compared with reference phases (Figure 7b), the crystalline ASR products (ES2_pt3 and Mels1_pt1), highly resemble shlykovite but not mountainite. This suggests that shlykovite is a better structural analogue to the crystalline ASR products. On the other hand, the spectra of the amorphous region (N1_pt6 and ES2_pt7) are highly comparable to that of K_CSH (C-S-H containing potassium) and other reported data of nano-crystalline C-S-H (CSH* [62]), suggesting that the amorphous ASR products are similar to C-S-H. This finding is further confirmed by the K and Na *K*-edge spectra; see details in [63].

The micro-XRD data (Figure 7c) further suggest that crystalline SKC, SNC and the field products are similar to shlykovite. However, peaks seem broadened in the ASR products. The relative intensity of their basal peaks are also smaller than that of shlykovite. This indicates a small crystallite size for the lab-synthesized products and even smaller for the field products, especially perpendicular to the silicate layer, i.e. along the *c*-axis. This matches the nano-platy morphology of both field ASR samples and lab-synthesized samples.

Meanwhile, the field samples exhibit multiple basal peaks (red square in Figure 7c) ranging from d~8.6 to ~13.4 Å, whereas shlykovite, SKC and SNC has only one basal peak (d~13.6 Å). A Rietveld refinement was applied to the XRD of Mels_pore, starting from the shlykovite structure, which resulted in a, b, c and β to be 6.63 Å, 6.51 Å, 23.37 Å and 85.3°. Compared to the lattice parameters of shlykovite (a = 6.49 Å, b = 7.00 Å, c = 26.71 Å and β = 94.6°), the unit cell in the field samples is slightly elongated along the a-axis, but shortened along the b-axis. The interlayer spacing of the field sample is about 1.1 Å shorter than that of shlykovite. The β angle also decreases by ~9.3°. Their configurational difference is illustrated by a shear glide between the adjacent layers along the a-axis (Figure 7d). The readers are referred to [61] for more details of the refinement.

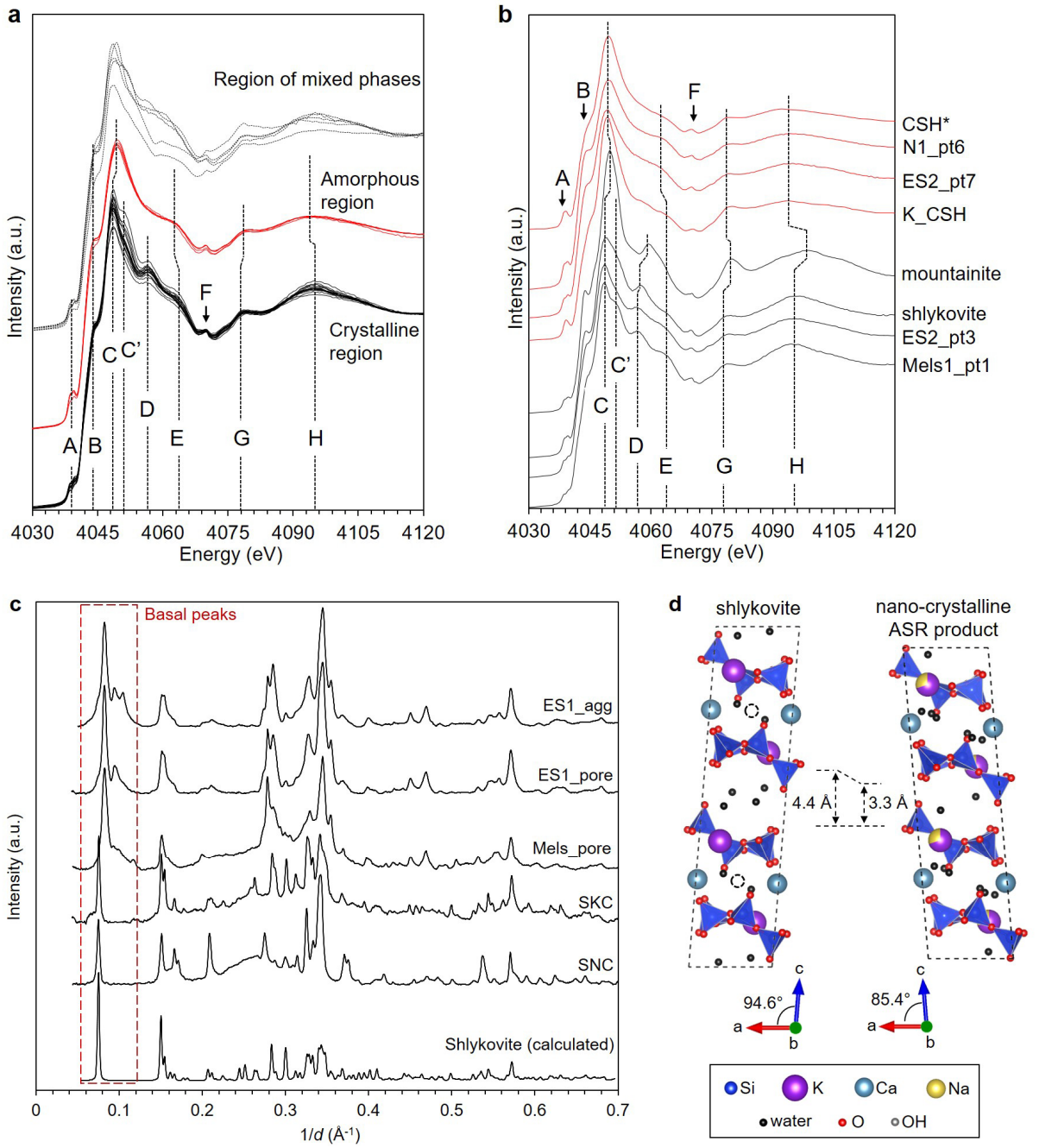

Figure 7. (a) The Ca K-edge XAS of the ASR products in an ASR-damaged concrete, (b) and the comparison with reference minerals and lab-synthesised ASR products. (c) The XRD of field ASR samples (ES1_agg, ES1_pore, Mels_pore), lab-synthesised sample (SKC, SNC) and shlykovite (theoretical calculation). (d) The postulated structure of crystalline ASR product in comparison with shlykovite (adapted from [61]).

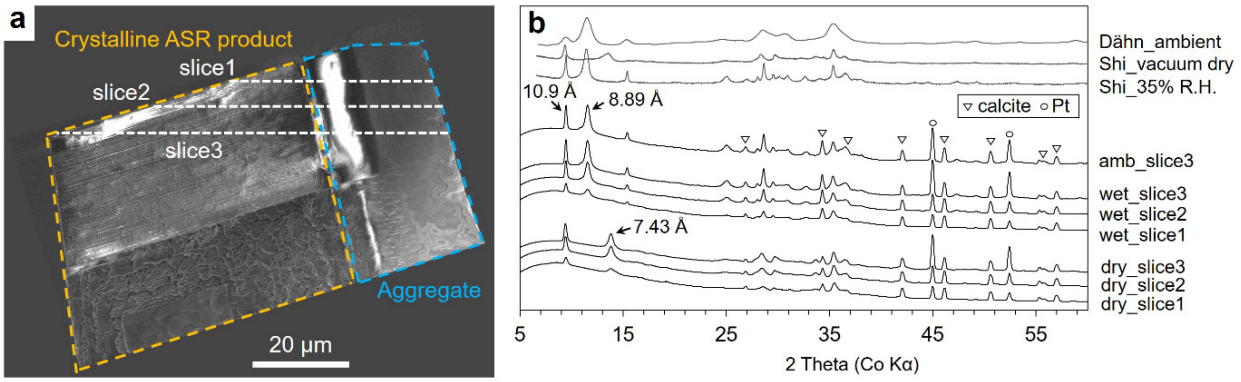

Figure 8. (a) SEM image of the FIB-extracted sub-volume for 3D tomographic XRD study. (b) The XRD of the three slices (white dashed line in a) compared with reported results by Dähn et al. [65] and Shi et al. [64] (adapted from [56]).

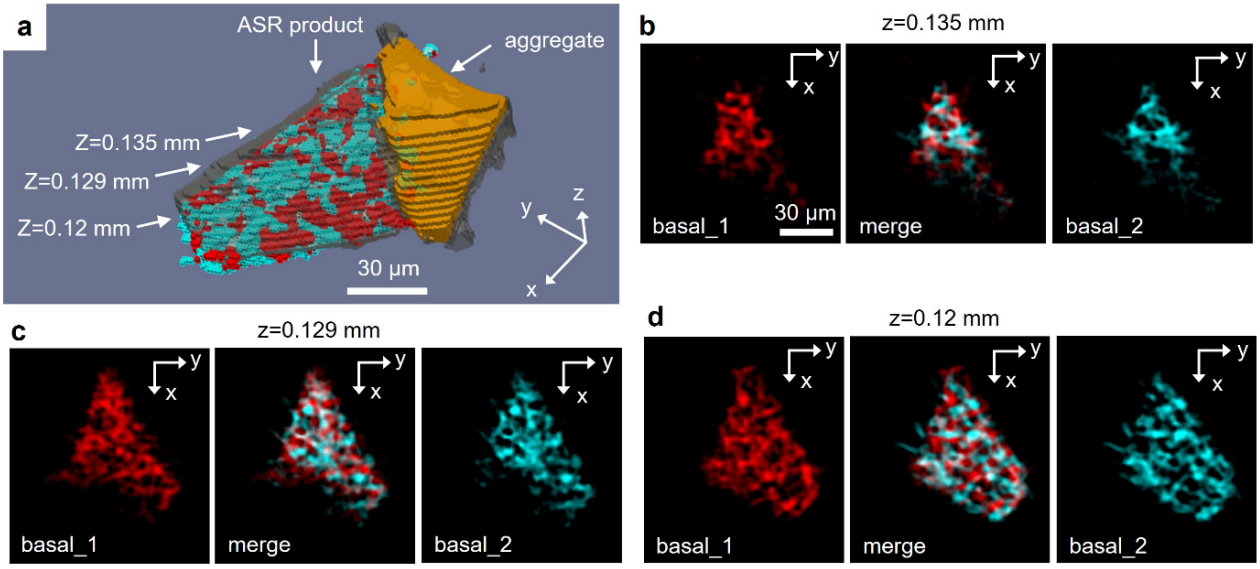

Figure 9. (a) Reconstructed distribution of basal_1 and basal_2 in the ASR product vein at RH ~ 10% in 3D view and (b-d) planar view at various vertical locations. The scale bar in b also applies to c and d (adapted from [56]).

5.2.2 Volume change of the product under various moisture conditions

The layered-structure and the multiple observed basal spacings together suggest the possibility of swelling/shrinking of ASR products during wetting/drying, which for decades has been postulated as a micro-mechanism of ASR damage. To validate this phenomenon, a 3D tomographic XRD study was conducted on a sub-volume extracted from a field sample, which contains an ASR product vein inside a calcite aggregate (Figure 8a). In this scanning method, XRD data is collected for each vertical slice (1.2-1.5 µm thick) at each rotation angle. The diffractogram of three slices are plotted together with reported results (Figure 8b). The diffractogram contains peaks from ASR products, calcite and Pt (from welding in FIB extraction). When the sample is in wet (RH ~97%) and ambient condition (RH ~38%), the XRD from ASR products in three slices are identical, and resemble the previously reported XRD of field samples [59] and synthesized samples at 35% RH [64]. Two basal peaks at 10.90 Å and 8.89 Å are observed. Even when the sample is in very dry condition (RH ~ 10%), the 10.9 Å basal peaks remains unchanged, while the 8.89 Å peak shifts to 7.43 Å. This is also observed for the synthesized sample at vacuum-dried condition [64].

The distinct behaviour of the 10.90 Å and 8.89 Å basal peaks suggests the existence of two ASR crystalline phases, one with a constant basal spacing (hereafter named phase basal_1) and the other with a varied basal spacing (basal_2) under varied RH. Using the 10.90 Å and 8.89 Å peak intensities, the distribution of basal_1 and basal_2 are reconstructed (Figure 9). When plotted together with the total solid volume reconstructed by Ca florescence signal (grey for ASR product and orange for aggregate), basal_1 (red) and basal_2 (cyan) inter-grow into each other and together occupy the volume of the ASR product vein (Figure 9a). The 2D map of basal_1 and basal_2 at various vertical positions (Figures 9b-d) further suggest that these phases are indeed distributed at distinct micro-locations. In other words, they must be different phases.

To further investigate the swelling of basal_2 to the overall volume change of the ASR product vein, the reconstructed volume of the basal_1 and basal_2 were calculated as a function of RH (Figure 10a and 10b). It seems that the volume of both phases remain nearly unchanged despite the change in RH from 10% to 97%, although XRD confirms that basal_2 basal spacing enlarges when RH is above ~38%. An explanation to this phenomenon is proposed in Figure 10c. The crystalline ASR products exist as agglomerated nano-platelets, within which a large amount of gaps is present. The swelling of the basal_2 platelets is accommodated by the gaps between the platelets, thus does not cause obvious change to the volume of the ASR product vein.

5.3 Summary and conclusions

The following conclusions can be drawn from the results of subproject III:

- The late-stage ASR-damaged concrete contains ASR products in both nano-crystalline and amorphous form. The nano-crystalline ASR products exhibit a crystal structure that highly resembles shlykovite – a layered silicate mineral. The amorphous ASR products are structurally similar to C-S-H at the molecular scale.
- The crystalline ASR products differ from the natural shlykovite in the stacking behaviour of the calcium alkali silicate layer. The basal spacing in the ASR product varies from 7.4 Å to 14 Å. The adjacent layers in the crystalline product of field samples may glide along the *b*-axis, resulting in a change in the β angle compared with shlykovite.
- ASR products of different basal spacings may co-exist in the product vein. Some products have constant basal spacings despite the change in RH, whereas the others exhibit basal spacing swelling when the RH increases from 10% to 35%, but not at higher RH relevant for ASR-affected concrete. The whole product vein, however, does not exhibit volume change during the wetting process.

6 Subproject IV: Synthetic ASR products

6.1 Introduction

Understanding about ASR is limited due to the lack of knowledge about the ASR products formed in concrete. One of the main challenges originates from insufficient characterizations of the ASR products. Since ASR products causing expansion are mainly formed in micro-scale veins of concrete aggregates, they cannot be sampled in sufficient amounts for characterizations with various conventional lab techniques. In subproject IV, both crystalline and amorphous ASR products comparable in composition and structure to those formed in concrete aggregates are synthesized at 20, 40, 60, and 80 °C [55,64]. The successful synthesis of these ASR products (at the gram-scale) allows, for the first time, a comprehensive characterization of ASR products using various lab techniques. By re-dissolving the synthesized ASR products, solubility data have also been obtained, which allow the prediction of the chemical boundaries for the formation of different types of ASR products [53,64,66].

6.2 Results: synthetic ASR products

6.2.1 Structure of crystalline ASR products formed at 80 °C

Based on the characterizations of the synthetic ASR products with various methods, it is found that the structures of all the synthesized crystalline ASR products at 80 °C are very similar. They are closely related to the crystal structure of the natural mineral shlykovite, which has a layered silicate structure with its SiO_4^{4-} tetrahedron charge-balanced by K^+ and Ca^{2+} in the main layer and by H^+ in the interlayer as shown in Figure 11 [57,67]. The structures of amorphous ASR products are more complicated: they may have a structure close to C-S-H if rich in Ca, or a short-ordered structure between C-S-H and crystalline ASR products according to ^{29}Si NMR and Raman spectra [53,55,66]. The structure of amorphous ASR products is not resolved at present. The synthesized crystalline and amorphous ASR products are consistent with the platy and granular products observed in concrete samples as elaborated in subproject II.

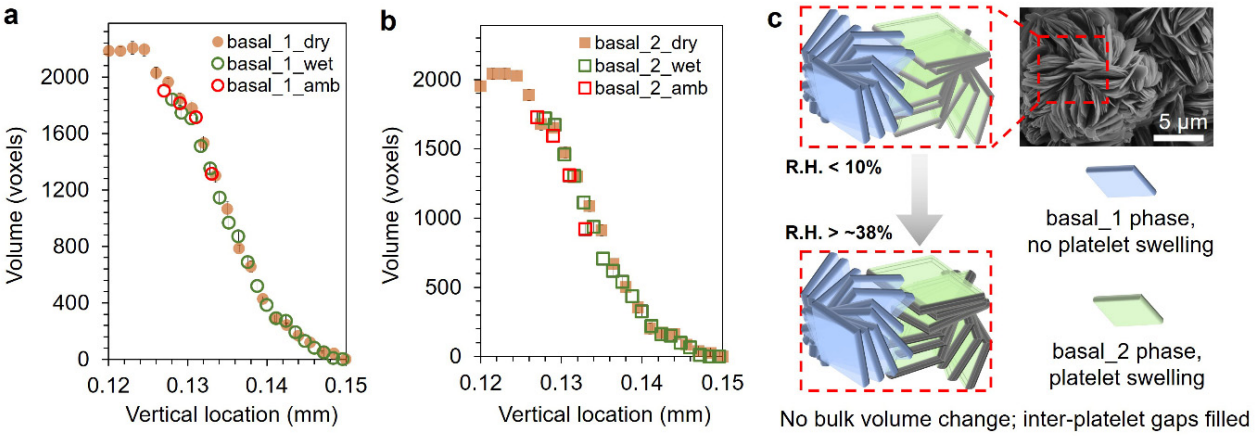

Figure 10. (a) The total volume (in voxel counts) of phase basal_1 and (b) basal_2 at each vertical slices of the studied sub-volume as a function of the moisture condition. The proposed micro-morphological change of the ASR product vein during wetting (adapted from [56]).

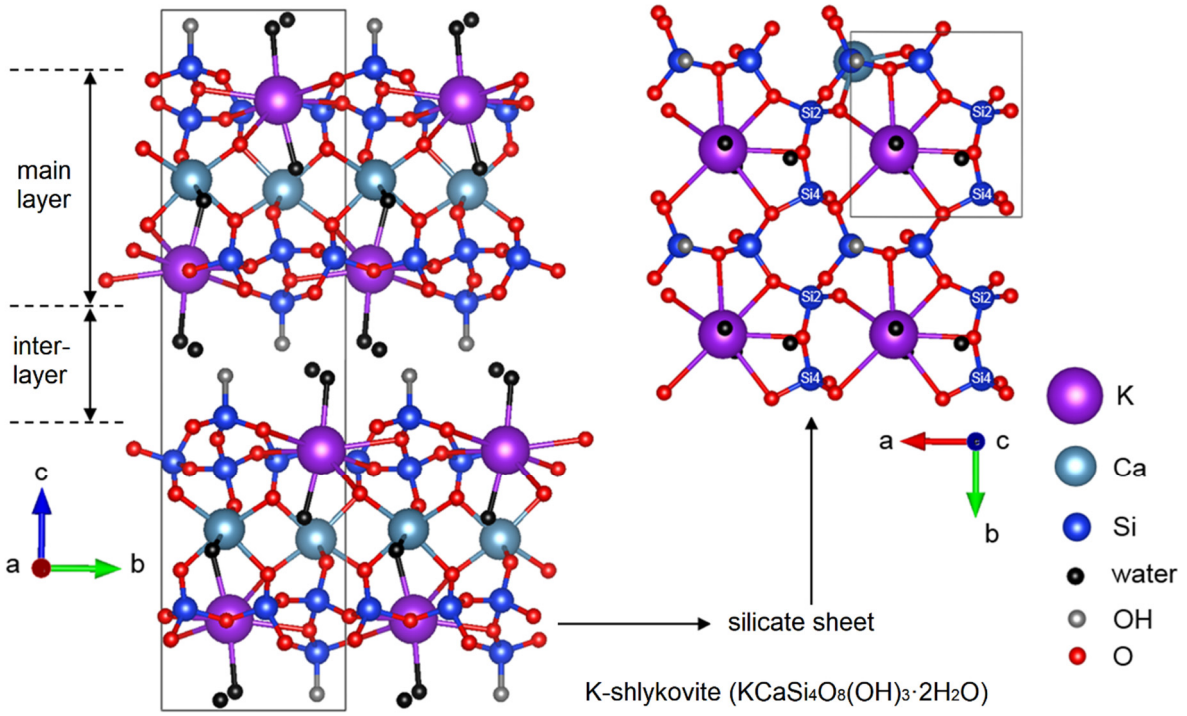

Figure 11. A schematic structure of shlykovite reproduced from [55,67], (a) viewed along [100], (b) the potassium silicate layer viewed along [001].

6.2.2 Effect of temperature and alkalis on the structure of crystalline ASR products

The temperature and type of alkalis are found to significantly affect the structure of crystalline and amorphous ASR products. For the samples containing K as the only alkali as shown in Figure 12, K-shlykovite with a basal spacing of 13.1 Å is only formed at elevated temperatures between 60 and 80 °C corresponding to accelerated ASR tests [55,68] or in concrete exposed to intense solar radiation [59]. At temperatures between 20 and 40 °C [64], the crystalline ASR product with a basal spacing of 10.8 Å is formed instead, which resembles the ASR products formed in field concrete at ambient temperature [56,69]. If also Na is present in addition to K, it affects the structure of the crystalline ASR products in different ways depending on the temperature. At a high temperature, e.g. 80°C, increasing the amount of Na will lead to the formation of ASR-P1, which is a nanocrystalline ASR product rather than K-shlykovite. If only Na is present, Na-shlykovite with a similar structure to K-shlykovite is formed [55]. Despite their very similar structures, their formation does not seem to be related to a cation exchange process, since they cannot form at the same time within the same concrete exposed to mixtures of KOH and NaOH solutions [68]. At lower temperatures, the precipitation of crystalline Na-ASR products is highly dependent on kinetics (unpublished data). The formation of Na-shlykovite is still observed when the temperature is reduced to 60 °C. However, at temperatures between 20 and 40 °C, precipitation of crystalline Na-containing products becomes more difficult, and mainly amorphous ASR products are formed. At 20 and 40°C, the structure of the 10.8 Å ASR product is affected and an increase of basal spacing from 10.8 Å up to 12.2 Å is observed if Na is added on top of K. This could be related to the entering of Na into the interlayer of 10.8 Å ASR product. Nevertheless, both types of products are formed in aggregates of field concrete structures [56,59,69]. For all crystalline ASR products with the same type of alkali (K or Na), their short-ordered structures are very similar as seen from Raman spectroscopy (Figure 12b), despite their differences in long-ordered structure as seen in XRD patterns (Figure 12a).

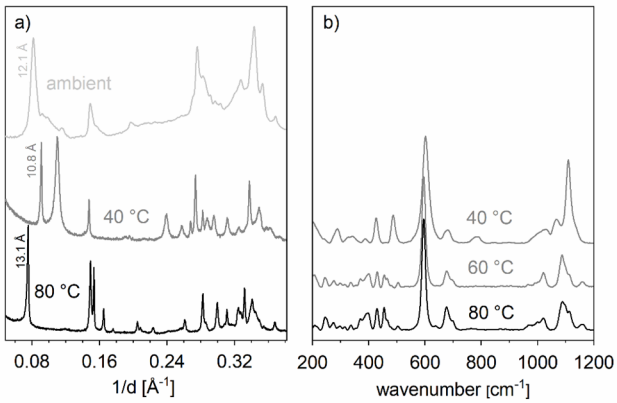

Figure 12. Effect of temperature on types of formed ASR products: (a) XRD patterns for the ASR products formed at 80 °C (13.1 Å), 40 °C (10.8 Å) and ambient condition (12.1 Å); (b) Raman spectra for the ASR products formed at 80 °C, 60 °C and 40 °C. Adapted from [64].

6.2.3 Water uptake capacity and swelling

According to the water-sorption results from DVS, all the synthesized crystalline ASR products 10.8 Å (20 – 40 °C, Figure 13), 13.1 Å (60 – 80 °C, K-shlykovite in Figure 13) and 12 Å (20 – 40 °C, unpublished data) show comparable or even lower water uptake than the C-S-H phase. This suggests that swelling of the studied crystalline ASR products by uptake of water cannot be the main mechanism of ASR-induced expansion. More details can be found in published studies on the synthesized samples [55,64]. This very limited water uptake is confirmed by micro-XRD and DVS of ASR products formed in ASR-affected structures [56,59].

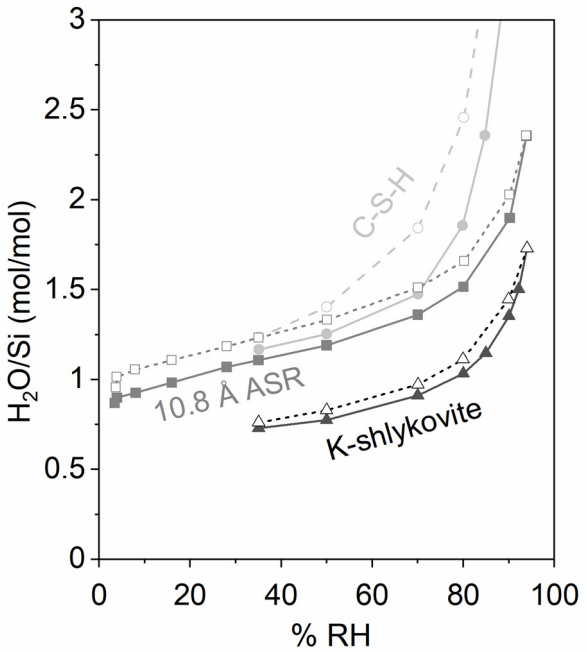

Figure 13. Sorption and desorption (dashed lines) isotherm for the ASR products formed at 80 °C (K-shlykovite), 40 °C (10.8 Å), and a reference sample of calcium-silicate-hydrate (C-S-H with Ca/Si ratio of 1.6) from 3 to 94 % RH. Adapted from [64].

6.2.4 Thermodynamic modelling of chemical boundaries for ASR

The chemical boundaries for the formation of ASR products can be assessed by thermodynamic modelling using the experimental derived thermodynamic data for shlykovite and amorphous ASR products [53,66]. Both experimental studies and thermodynamic modelling confirm that alkalis and calcium play essential roles in the formation of ASR products. Figure 14 shows such the effect of Ca and alkali based on thermodynamic modelling at 80 °C. The presence of Ca (at a fixed alkali/Si ratio of 0.5) increases the formation of ASR products at low dosages (<0.2 Ca/Si), but at higher Ca/Si ratio, ASR products are converted to C-S-H. At a fixed Ca/Si ratio of 0.3, a sufficient amount of K or Na is needed for the formation of ASR products, while at low alkali/Si ratio, C-S-H is stabilized instead. However, too high alkaline content K(or Na)/Si $\geqslant 1$ also favours C-S-H formation and suppresses the formation of ASR product, due to a strong effect of the alkalis (K and/or Na) on calcium concentrations.

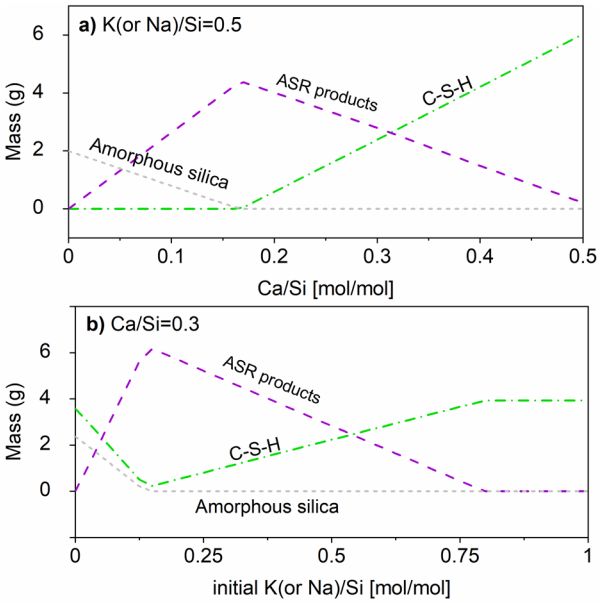

Figure 14. Chemical boundaries for the formation of ASR products: a) effect of alkali/Si ratio, b) effect of Ca/Si ratio. The symbols on the dashed lines are data calculated from thermodynamic modelling. Adapted from [66].

6.3 Discussion

At 60 and 80 °C, crystalline ASR products with a shlykovite-like structure and amorphous ASR products are formed both in laboratory experiments and field studies. Temperature affects the crystal structure of crystalline ASR products. The combination of the XRD and Raman data suggests that the main changes occur on the long-ordered structure, i.e. the basal spacing of the crystalline ASR products, whereas the short-ordered structure remains very similar, in particular at lower temperature range (20 – 40°C), whose Raman shifts are even identical. All crystalline ASR products formed at different temperatures have a layered silicate structure similar to shlykovite formed in natural rocks. None of the crystalline ASR products can swell significantly, since their water-uptake is very much limited, similar or even less than the water-uptake of C-S-H. Therefore, swelling upon water uptake cannot be the main mechanism of ASR-induced concrete expansion.

Thermodynamic modelling shows that ASR products are formed within specific chemistry boundaries. The optimum Ca/Si ratio and alkali/Si ratio for the formation of ASR products are within the range of 0.1 – 0.3. This chemical boundary agrees very well with the experimental observations that ASR products favourably form within concrete aggregates, where the calcium content is limited compared to the large reservoir of calcium in cement pastes. This is not in contradiction with the few scenarios where ASR products are observed in air voids or ASR products formed where silica fume is agglomerated [68,70]. It also explains why ground aggregates cause less ASR expansion [2], since the reactive components are in direct contact with a large amount of calcium from hydrated cement pastes. This suggests that a micro-environment like the interior of aggregates is critical for the occurrence of ASR, where ion

gradients occur across from the paste to the interior of the aggregates. Therefore, the transport of the alkalis and calcium ions into aggregates also controls the rate of ASR kinetics as also proposed earlier by other researchers [71].

6.4 Summary and conclusions

The synthesis of ASR products allows their analysis with conventional characterization techniques revealing the following insights:

- Both crystalline and amorphous ASR products identical to those formed in concrete aggregates are successfully synthesized: at 20 - 40 °C, 12.0 Å and 10.8 Å ASR products form, while at 60 – 80 °C, 13.1 Å ASR products (= shlykovite) and amorphous ASR-P1 forms.
- All crystalline ASR products exhibit a sheet-like structure similar to the natural mineral shlykovite.
- The water uptake capacity of crystalline and amorphous ASR products during the wet-dry cycles is smaller or comparable to C-S-H phases. This suggests that swelling of the studied ASR products by uptake of water cannot be the main mechanism of ASR-induced expansion.
- Both experimental studies and thermodynamic modelling show an "optimum" Ca/Si and alkali/Si ratios of ≈0.2 for the formation of ASR products, while at higher and lower ratios either SiO_2 or C-S-H is formed, which agrees well with the observation that ASR products are mainly formed within concrete aggregates and degraded to C-S-H when extruded into cement paste.

7 Subproject V: ASR products and cracking - a 4D view

7.1 Introduction

The chemo-mechanics of ASR damage, i.e., the couplings between ASR products evolution and concrete cracking, was investigated at concrete's meso-scale via time-lapse XT customized for ASR studies. We optimized X-ray attenuation contrast enhancers for better distinguishing among the various material phases. We used $CsNO_3$ [72] and $BaSO_4$ for enhancing the contrast between the ASR products and all other phases and between the cement paste and the aggregates, respectively. Such optimization allowed the development of 3D image processing workflows for the quantitative analysis of the mentioned chemo-mechanics [72].

7.2 Results: ASR products accumulation and crack propagation

Figure 15 exemplifies how the developed methodology empowers the time-lapse investigation of ASR cracking. It shows a time series of tomograms for one specimen. The aggregates are clearly distinguishable from the paste. They appear much darker (i.e., with smaller X-ray attenuation) than the paste, which contains the well-dispersed $BaSO_4$. Compared with typical X-ray tomograms of concrete [73,74], the aggregate segmentation is simpler and much more reliable for our tomograms.

The process observable in Figure 15 consisted of the gradual accumulation of products within a delaminated part of the ITZ of an aggregate and within a nearby micro-crack close to the ITZ. Both existed already at the start of the ASR acceleration. They had size close to the tomographic spatial resolution (Figures 15a-c). The accumulation was very clear because of the extremely higher X-ray attenuation by the Cs-doped products compared with the other material phases (very bright regions in Figures 15d-f). It was accompanied by widening of the delaminated ITZ and its continuation into the paste as a crack (Figures 15e-f). The products were extruded from the aggregate into the paste along the newly propagated crack. Additional crack propagation through the paste occurred also from another side of the same aggregate, where the ITZ was originally not delaminated. However, less products extrusion took place from that side. The described processes (crack lengthening/widening and products extrusion) and their couplings can be better appreciated by watching the full tomographic time series, of which Figure 15 is just an excerpt (movie in the Supplementary Data).

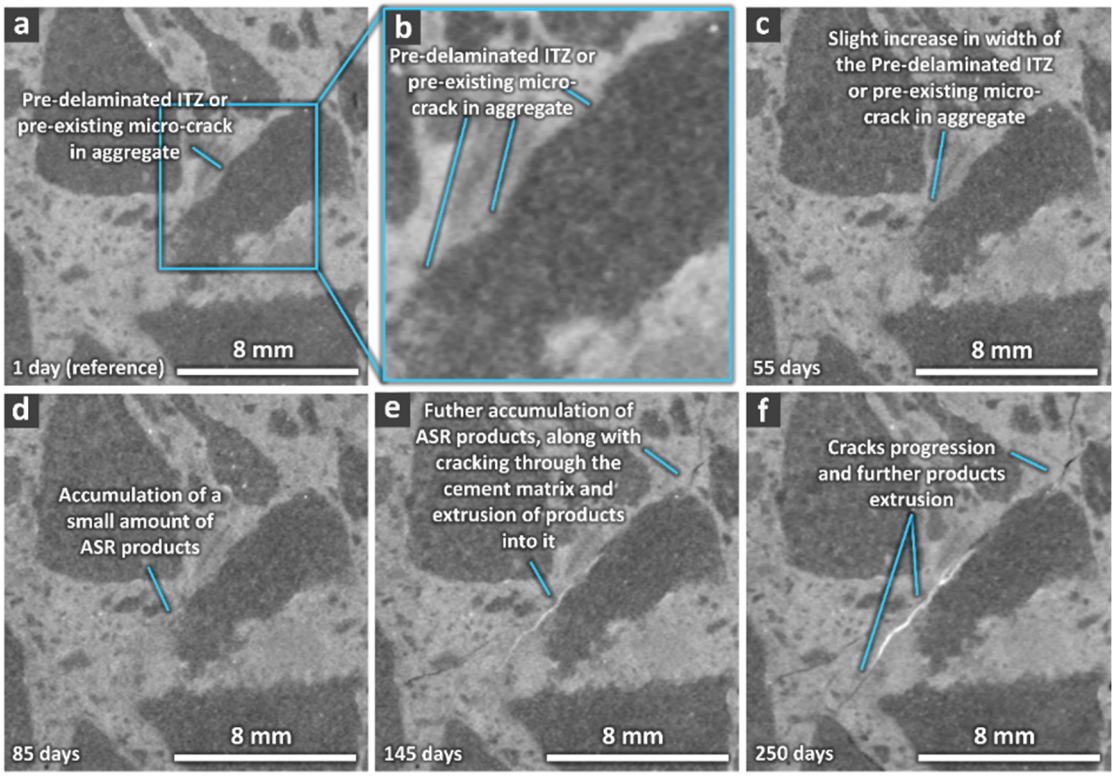

Figure 15. 2D cross-section ("slice") from a 3D ROI of the (registered) time-lapse X-ray tomograms of a specimen cast with U aggregates (calcareous sandstone, see S5.1) and with $BaSO_4$ and $CsNO_3$ as contrast enhancers. ASR products are visible as very bright regions, because of Cs-doping, within cracks and near the aggregate boundaries. The slices shown here are from the tomograms at (a) and (b) 1 day, (c) 55 days, (d) 85 days, (e) 145 days and (f) 250 days from the start of the ASR acceleration protocol.

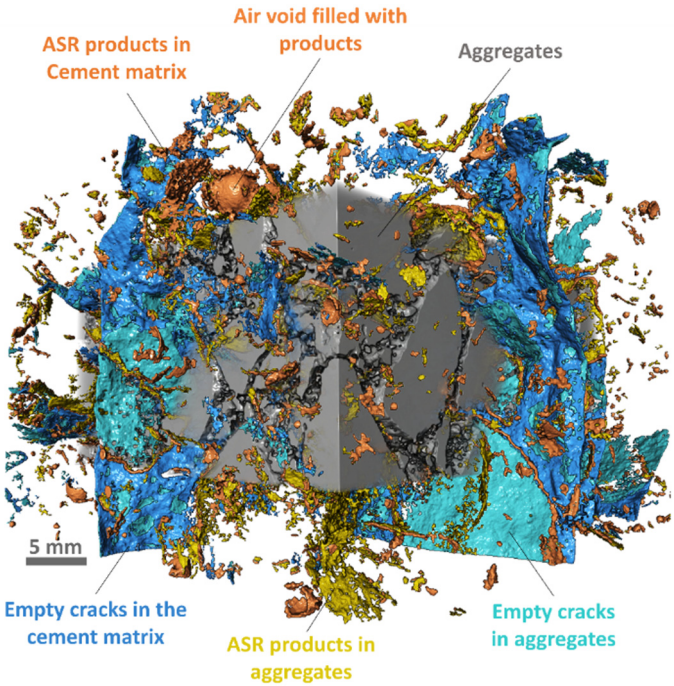

Figure 16. 3D rendering of the volumes of the segmented empty cracks inside aggregates (in cyan) and inside the cement matrix (in blue), respectively, and of the segmented ASR products, distinguishing between inside aggregates (in yellow) and inside the cement matrix (in orange) as well. Only part of the volume of the segmented aggregates is shown in semi-transparent grey, to allow seeing the extent of the other volumes. Notice that part of the products volume did not consist of cracks but of other types of pores, e.g., air voids. The specimen was the same as for Figure 15 and the tomogram in the time series was the one at 250 days.

An example of the advantages brought by the two types of contrast enhancement and by the developed 3D image analysis is showcased in Figure 16. There, the volumes of the distinct, segmented phases (aggregates and ASR products) and of the empty cracks are 3D rendered. The aggregates' volume was partially cropped and rendered in semi-transparent grey, to allow seeing the full extent of the other volumes. The latter were rendered as opaque solids with distinct colors. The coloring does not only distinguish the volumes. It also indicates whether the cracks and products were within the aggregates or the paste. Such segmentation results allowed determining that the ASR products occurred extensively not only inside aggregates, as expectable, but also within the paste. A significant amount of ASR products accumulated within the air voids as well.

7.3 Discussion

The developed methodology has empowered new qualitative and quantitative characterization of ASR damage. For example, evidence of ASR products transport from the aggregates into the paste has been already available in the literature since decades, in the form of 2D images of cracks and air voids filled with products [75-78]. However, our developed methodology has allowed time-resolved, 3D observations of that process with higher products visibility [72]. In addition, the quantitative estimates of similar volumes of empty and filled cracks supports the hypothesis of a significant degree of product mobility. These results point to relatively low viscosity of ASR products, at least until late stages. Such feature may play a significant role in the ASR cracking and would need to be integrated in its computational models.

The spatial resolution of our tomograms (70 µm) did not detect the early-stage products, whose size is in the sub-micrometer range [13]. Thus, we could not assess the causal relations between products accumulation/transport and crack opening and propagation (Figure 15). Our methodology, applied on very small model systems, would bridge the gap between the non-time-lapse observations of early-stage products by 2D electron microscopy methods and the late stage, meso-scale observations reported here. This remains a needed step in direction of elucidating the root causes of the early cracking.

7.4 Summary and conclusions

By the developed methodology, it was possible to observe, for the first time and while unfolding, the co-occurrence of crack propagation from the aggregates into the cement paste and the impulsive extrusion and transport of products along the cracks, up to several millimeters away from the originally cracking aggregates [72]. The developed 3D image analysis workflows allowed quantifying geometrical crack features [72]. These results, along with the availability of time-lapse 3D digital models of the concrete meso-structure and of the crack networks, support the meso-scale computational modeling in subproject VI.

8 Subproject VI: Numerical modeling of mechanics

8.1 Introduction

Sub-project VI explores the nature of expansion and cracking of ASR-affected concrete by analytical and numerical modeling. ASR is considered at a wide range of scales: from a nanometer-thick layer of initial ASR-product within an aggregate up to a few hundred meters long ASR-affected concrete dam. Principal research questions comprise identification of the mechanism of crack opening and growth, investigation of the role of creep on damage extent as well as the source of the anisotropy in expansion of concrete [79,80]. Another important research question is the coupling between the mesoscopic ASR manifestations (local expansion and cracking) and the macroscopic behavior of concrete structures, namely dams [81]. The nano-scale part of the research is omitted for brevity, and the meso- and macro-scale studies are discussed. Details on the nano-scale study are available in [82].

8.2 Results: Numerical modeling of ASR mechanics

8.2.1 Meso-scale

At the meso-scale, the principal questions addressed are concerning the crack opening and propagation mechanisms, the source of anisotropic ASR-expansion under different loading conditions, and the role of the cement paste creep on the cracking extent. The meso-scale studies could be further split into two subgroups based on the crack modelling approach.

In the first study, both two- and three-dimensional finite-element models of concrete internal structure are implemented [79,80]. In these models, concrete aggregates, paste, and ASR-product pockets are explicitly simulated. The latter are represented by separate finite elements randomly distributed within aggregates. Their gradual expansion imposes internal pressure on the surrounding matrix leading to the evolution of cracks. The softening behaviour of cracked aggregates and paste are modelled by a continuum damage model. This damage model aims at simulating the reduction of the material stiffness by considering the evolution of a scalar damage variable *D*. While the mechanical behaviour of the aggregates is described by a strain softening constitutive law, it is combined with viscoelasticity to describe the mechanical behaviour of the paste. Internal loading from ASR products is applied together with either external free expansion boundary conditions or uniaxial external load.

This study allowed evaluating the effect of material constitutive law, elastic properties of material phases, percentage of ASR reaction products, and temperature on global response of ASR-affected concrete. It was shown that the major part of the macroscopic expansion is due to the damage generation and cracks opening, and only a minor part is due to the elastic deformation. The introduction of viscoelasticity in the paste resulted in the reduction of the damage levels in the paste, while keeping high levels of deformation. The increase in numbers of active ASR sites has

an increasing effect on the specimen expansion rate and the final expansion value. It also gives rise to a higher amount of damaged volume in both phases.

In contrast to the previous approach, in the second study cracks were modelled by cohesive elements - zero-thickness elements placed at a material interface. Application of the internal load leads to the evolution of complex crack networks.

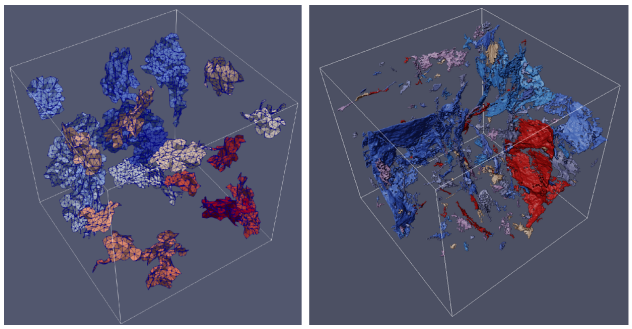

Figure 17. Numerically computed cracks in concrete specimen (on the left) next to their experimental counterpart.

A typical crack pattern is shown in Figure 17 together with its experimental counterpart. The proposed approach allows modeling multiple cracks within an irregular mesh. Each crack is numbered individually, which simplifies collection of statistics and visual inspection. Although all of them begin with almost flat shapes, later they deviate from the initial direction, branch and merge, developing complex 3D-shapes and networks. Each individual crack trajectory strongly depends on the local material composition, loading profile, proximity of other cracks, meshing, etc. As it is not possible to exactly match the crack network observed in the laboratory experiments, two sets of statistics are compared instead. The latter comprise distributions of such parameters as the crack surfaces, volumes, and orientations. Similar statistics were collected from the tomography data on ASR-damaged concrete specimens by the colleagues from subproject V. Comparison between numerical and experimental sets of data and adjusting the model parameters for better matching is subject of current work.

8.2.2 Macro-scale

The goal of the macro-scale study is to understand the coupling between the meso-scale processes with the macroscopic structure behaviour. Additionally, the role of temperature on the macroscopic concrete deterioration is investigated. For this purpose, a two-dimensional multi-scale model comprising meso- and macro-scales was developed (see Figure 18).

At the macro-scale, a typical ASR-affected structure such as a dam could measure hundreds of meters in size discretized with finite elements with dimensions of a couple of meters. Each integration point of such finite element has an underlying meso-scale problem of few centimetres size. The fine-scale problem, also called representative volume element (RVE), serves as a constitutive equation for the macro-scale problem.

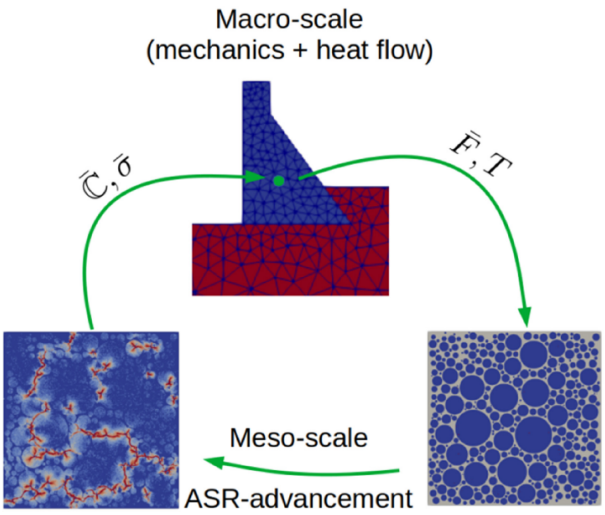

Figure 18. Schematic illustration of the multi-scale scheme for ASR simulations.

The major result is the proof of the model applicability to the ASR problems. Although the evolution of the percolated crack bands within RVEs is evident, their diffused patterns make the classical homogenization concept still applicable. Validation of the model is done by comparison with the experimental data. The obtained results (global expansion and stiffness reduction) are in fair agreement with the laboratory data.

The results demonstrate that the macroscopic stress state influences the orientation of damage inside the underlying RVEs and therefore the anisotropy of expansion. The effective stiffness becomes anisotropic in cases where damage is aligned inside an RVE. An example of such aligned cracks is shown in Figure 19. More details on the model implementation and verification can be found in [81]. The model is developed within the open-source parallel FE library Akantu [83].

Figure 19. Damage map within an RVE under uniaxial compression load of 10 MPa. Arrows denote the loading direction.

8.3 Summary and conclusions

The numerical models developed in this project cover a wide range of scales. They provided a close look to specific phenomena such as crack initiation, propagation and

percolation. The availability of the model data at different scales allowed linking between micro-scale processes with their macroscopic manifestations, such as expansion and stiffness loss. The roles of material behavior including creep, sizes of inclusions, and loading amplitude were studied and corresponding conclusions were made. Tomography data from subproject V was used to build the numerical model and to compare the obtained results. While a qualitative match between numerical and experimental crack patterns is evident, matching the two sets of statistical data is subject of current work.

9 Outlook

The selected highlights of the Sinergia project underline the benefits of a multidisciplinary research approach. The results represent a starting point for further explorations in the field of ASR. There is a wide range of additions that have the potential to decrease SiO_2 dissolution [84-86]. Their applicability in concrete production has still to be explored. While the knowledge on the crystalline ASR products has been significantly improved in the project, the characteristics of the initially formed amorphous ASR products and their transition to a nanocrystalline material remain difficult to capture. As they may represent a key point for understanding the mechanism of stress generation, further research should provide insights on their structure and on their thermodynamics. The combination of FIB with TEM, synchrotron-based methods and synthesis as chosen in this project is a promising approach that deserves to be explored further. The developed technique to provide a spatial and time resolved view of ASR products and cracking can be extended from the mesoscale both to the microscale and to larger scales, providing an extended data base for the development of numerical modeling. After having succeeded to reproduce realistic crack patterns by numerical modeling, the ongoing challenge remains to adjust the model components to obtain similar crack statistics.

Acknowledgments

The authors would like to thank Swiss National Science Foundation (SNF Sinergia, grant number CRSII5_17108) for funding the project.

Authorship statement (CRediT)

Andreas Leemann: Conceptualization, Writing – original draft, Writing – review and editing, Project administration

Mahsa Bagheri: Investigation, Writing – original draft

Barbara Lothenbach: Conceptualization, Writing – review and editing, Supervision

Karen Scrivener: Conceptualization, Writing – review and editing, Supervision

Solène Barbotin: Investigation, Writing – original draft

Emmanuelle Boehm-Courjault: Conceptualization, Writing – review and editing, Supervision

Guoqing Geng: Investigation, Writing – original draft

Rainer Dähn: Conceptualization, Writing – review and editing, Supervision

Zhenguo Shi: Investigation, Writing – original draft

Mahdieh Shakoorioskooie: Investigation, Writing – original draft

Michele Griffa: Conceptualization, Investigation, Writing – review and editing, Supervision

Robert Zboray: Investigation, Resources

Pietro Lura: Conceptualization, Writing – review and editing, Supervision

Emil Gallyamov: Investigation, Writing – original draft

Roozbeh Rezakhani: Investigation, Writing – original draft

Jean-Francois Molinari: Conceptualization, Writing – review and editing, Supervision

Declaration of interest

The authors declare that they have no known competing financial interests or personal relationships that could have appeared to influence the work reported in this paper.

References

[1] R.N. Swamy (Ed.), The alkali-silica reaction in concrete. CRC Press, 1991.
[2] H. De Mayo Bernardes, N.P. Hasparyk (Eds.), Proc 15th ICAAR, Sao Paolo/Brasil, 2016.
[3] A. Lopes Batista, A. Santos Silva, I. Fernandes, L. Oliveira Santos, J. Custódio, C. Serra (Eds.) Proc 16th ICAAR, Volume I, Lisbon/Portugal, 2021.
[4] L.S. Dent Glasser, N. Kataoka, The chemistry of "alkali-aggregate" reaction. Cem Concr Res (1981) 11: 1–9. https://doi.org/10.1016/0008-8846(81)90003-X.
[5] P.W.J.G. Wijnen, T.P.M. Beelen, J.W. De Haan, C.P.J. Rummens, L.J. M. Van de Ven, R.A. Van Santen, Silica gel dissolution in aqueous alkali metal hydroxides studied by ^{29}Si-NMR. J Non-Cryst Solids (1989) 109(1): 85-94. https://doi.org/10.1016/0022-3093(89)90446-8.
[6] A. Leemann, G. Le Saout, F. Winnefeld, D. Rentsch, D., B. Lothenbach, Alkali–silica reaction: the influence of calcium on silica dissolution and the formation of reaction products. J Am Ceram Soc (2011) 94(4): 1243-1249. https://doi.org/10.1111/j.1551-2916.2010.04202.x.
[7] T. Chappex, K.L. Scrivener, The influence of aluminium on the dissolution of amorphous silica and its relation to alkali silica reaction. Cem Concr Res (2012) 42: 1645–1649. https://doi.org/10.1016/j.cemconres.2012.09.009.
[8] F. Tiecher, M.E. Gomes, D.C. Dal Molin, N.P. Hasparyk, P.J. Monteiro, Relationship between degree of deformation in quartz and silica dissolution for the development of alkali-silica reaction in concrete. Mater (2017) 10(9): 1022. https://doi.org/10.3390/ma10091022.
[9] L.S.D. Glasser, N. Kataoka, On the role of calcium in the alkali-aggregate reaction. Cem Concr Res (1982) 12(3): 321-331. https://doi.org/10.1016/0008-8846(82)90080-1.
[10] P.W. Wijnen, T. P.Beelen, K.P. Rummens, R.A. Van Santen, The role of cations in the formation of aqueous silica gels. J Non-Cryst Solids (1993) 152(2-3): 127-136. https://doi.org/10.1016/0022-3093(93)90241-O.
[11] F. Gaboriaud, A. Nonat, D. Chaumont, A. Craievich, Structural model of gelation processes of a sodium silicate sol destabilized by calcium ions: combination of SAXS and rheological measurements. J Non-Cryst Solids (2005) 351(4): 351-354. https://doi.org/10.1016/j.jnoncrysol.2004.11.019.
[12] J.H.M. Visser, Fundamentals of alkali-silica gel formation and swelling: Condensation under influence of dissolved salts. Cem Concr Res (2018) 105: 18-30. https://doi.org/10.1016/j.cemconres.2017.11.006.
[13] A. Leemann, B. Münch, The addition of caesium to concrete with alkali-silica reaction: Implications on product identification and recognition of the reaction sequence. Cem Concr Res (2019) 120: 27-35. https://doi.org/10.1016/j.cemconres.2019.03.016.
[14] P. Gautam, D. K. Panesar, The effect of elevated conditioning temperature on the ASR expansion, cracking and properties of

reactive Spratt aggregate concrete. Constr Build Mater (2017) 140: 310–320. https://doi.org/10.1016/j.conbuildmat.2017.02.104.
[15] H. Kagimoto, Y. Yasuda, and M. Kawamura, Mechanisms of ASR surface cracking in a massive concrete cylinder. Adv Concr Constr (2015) 3(1): 39–54. https://doi.org/10.12989/acc.2015.3.1.039.
[16] A. Teramoto, M. Watanabe, R. Murakami, T. Ohkubo, Visualization of internal crack growth due to alkali–silica reaction using digital image correlation. Constr Build Mater (2018) 190:851-860. https://doi.org/10.1016/j.conbuildmat.2018.09.168
[17] R.N. Swamy, M.M. Al-Asali, Engineering properties of concrete affected by alkali-silica reaction. Mater J (1988) 85(5):367-374.
[18] S. Multon, J.F. Seignol, F. Toutlemonde, Structural behavior of concrete beams affected by alkali-silica reaction. ACI Mater J (2005) 102(2):67.
[19] G. Giaccio, R. Zerbino, J.M. Ponce, O.R. Batic, Mechanical behavior of concretes damaged by alkali-silica reaction. Cem Concr Res (2008) 38(7): 993-1004. https://doi.org/10.1016/j.cemconres.2008.02.009.
[20] C.F. Dunant, K.L. Scrivener, Micro-mechanical modelling of alkali–silica-reaction-induced degradation using the AMIE framework. Cem Concr Res (2010) 40(4): 517-525. https://doi.org/10.1016/j.cemconres.2009.07.024.
[21] A. Mohammadi, E. Ghiasvand, M. Nili, Relation between mechanical properties of concrete and alkali-silica reaction (ASR); a review. Constr Build Mater (2020) 258:119567. https://doi.org/10.1016/j.conbuildmat.2020.119567.
[22] T.E. Stanton, Influence of cement and aggregate on concrete expansion. Eng News Rec (1940):59-61
[23] T.E. Stanton, Expansion of concrete through reaction between cement and aggregate. Proc. Am Soc Civ Eng (1940) 66 (10):1781-1811.
[24] S. Diamond, Alkali silica reactions - some paradoxes. Cem Concr Compos (1997) 19(5-6):391-401. https://doi.org/10.1016/S0958-9465(97)00004-8.
[25] F. Rajabipour, E. Giannini, C. Dunant, J.H. Ideker, M.D.A. Thomas, Alkali-silica reaction: current understanding of the reaction mechanisms and the knowledge gaps. Cem Concr Res (2015) 76:130–146. https://doi.org/10.1016/j.cemconres.2015.05.024.
[26] A. Leemann, T. Katayama, I. Fernandes, M.A. Broekmans, Types of alkali–aggregate reactions and the products formed. Proc Inst Civil Eng Constr Mater (2016) 169(3), 128-135. https://doi.org/10.1680/jcoma.15.00059.
[27] M. Thomas, B. Fournier, K. Folliard, J. Ideker, M. Shehata, Test methods for evaluating preventive measures for controlling expansion due to alkali–silica reaction in concrete. Cem Concr Res (2006) 36(10):1842-1856. https://doi.org/10.1016/j.cemconres.2006.01.014.
[28] B. Fournier, J.H. Ideker, K.J. Folliard, M.D. Thomas, P.C. Nkinamubanzi, R. Chevrier, Effect of environmental conditions on expansion in concrete due to alkali-silica reaction (ASR). Mater Charact (2009) 60(7):669-679. https://doi.org/10.1016/j.matchar.2008.12.018.
[29] B. Fournier, R. Chevrier, A. Bilodeau, P.C. Nkinamubanzi, N. Bouzoubaa, Comparative field and laboratory investigations on the use of supplementary cementing materials (SCMs) to control alkali-silica reaction in concrete. Proc 15th ICAAR, Sao Paolo/Brasil, 2016.
[30] Y. Kawabata, K. Yamada, Y. Sagawa, S. Ogawa, Alkali-wrapped concrete prism test (AW-CPT) – new testing protocol toward a performance test against alkali-silica reaction. J Adv Concr Technol (2018) 16(9):441-460. https://doi.org/10.3151/jact.16.441.
[31] M. Bagheri, B. Lothenbach, M. Shakoorioskooie, A. Leemann, K. Scrivener, Use of scratch tracking method to study the dissolution of alpine aggregates subject to alkali silica reaction. Cem Concr Compos (2021) 104260. https://doi.org/10.1016/j.cemconcomp.2021.104260.
[32] S.L. Brantley, A.F. White, J.D. Kubicki, Kinetics of Water-Rock Interaction, 2008. https://doi.org/10.1007/978-0-387-73563-4.
[33] P.M. Dove, The dissolution kinetics of quartz in sodium chloride solutions at 25° to 300°C. Am J Sci (1994) 294:665–712. https://doi.org/10.2475/ajs.294.6.665.
[34] R. Wollast, L. Chou, Rate control of weathering of silicate minerals at room temperature and pressure. In: Physical and chemical weathering in geochemical cycles.Springer, Dordrecht (1988):11-32. https://doi.org/10.1007/978-94-009-3071-1.
[35] P.V. Brady, J.V. Walther, Kinetics of quartz dissolution at low temperatures. Chem Geol (1990) 82:253–264. https://doi.org/10.1016/0009-2541(90)90084-K.
[36] W.A. House, D.R. Orr, Investigation of the pH dependence of the kinetics of quartz dissolution at 25°C. J Chem Soc Faraday Trans (1992) 88:233–241. https://doi.org/10.1039/FT9928800233.
[37] L. Chou, R. Wollast, Steady-state kinetics and dissolution mechanisms of albite. Am J Sci (1985) 285:963–993. https://doi.org/10.2475/ajs.285.10.963.
[38] K.G. Knauss, T.J. Wolery, Dependence of albite dissolution kinetics on pH and time at 25°c and 70°c. Geochim Cosmochim Acta (1986) 50:2481–2497. https://doi.org/10.1016/0016-7037(86)90031-1.
[39] K. Lammers, M.M. Smith, S.A. Carroll, Muscovite dissolution kinetics as a function of pH at elevated temperature. Chem Geol (2017) 466:149–158. https://doi.org/10.1016/j.chemgeo.2017.06.003.
[40] K.G. Knauss, Muscovite dissolution kinetics as a function of pH and time at 70°C. Geochim Cosmochim Acta (1989) 53:1493–1501. https://doi.org/10.1016/0016-7037(89)90232-9.
[41] E.H. Oelkers, J. Schott, J. Gauthier, T. Herrero-Roncal, An experimental study of the dissolution mechanism and rates of muscovite. Geochim Cosmochim Acta (2008) 72:4948–4961. https://doi.org/10.1016/j.gca.2008.01.040.
[42] T. Chappex, K.L. Scrivener, The effect of aluminum in solution on the dissolution of amorphous silica and its relation to cementitious systems. J Am Ceram Soc (2013) 96:592–597. https://doi.org/10.1111/jace.12098.
[43] M. Bagheri, B. Lothenbach, M. Shakoorioskooie, K. Scrivener, Effect of different ions on dissolution rates of silica and feldspars at high pH. Cem Concr Res (2022) 152:106644. https://doi.org/10.1016/j.cemconres.2021.106644.
[44] P.M. Dove, C.J. Nix, The influence of the alkaline earth cations, magnesium, calcium, and barium on the dissolution kinetics of quartz. Geochim Cosmochim Acta (1997) 61: 3329–3340. https://doi.org/10.1016/S0016-7037(97)00217-2.
[45] P.M. Dove, The dissolution kinetics of quartz in aqueous mixed cation solutions, Geochim Cosmochim Acta (1999) 63: 3715–3727. https://doi.org/10.1016/S0016-7037(99)00218-5.
[46] W.J. McCOY, A.G. Caldwell, New approach to inhibiting alkali-aggregate expansion, ACI J Proc (1951) 47: 693–706. https://doi.org/10.14359/12030.
[47] X. Feng, M.D.A. Thomas, T.W. Bremner, B.J. Balcom, K.J. Folliard, Studies on lithium salts to mitigate ASR-induced expansion in new concrete: a critical review. Cem Concr Res (2005) 35: 1789–1796. https://doi.org/10.1016/j.cemconres.2004.10.013.
[48] M. Kawamura, H. Fuwa, Effects of lithium salts on ASR gel composition and expansion of mortars. Cem Concr Res (2003) 33: 913–919. https://doi.org/10.1016/S0008-8846(02)01092-X.
[49] X. Mo, Laboratory study of LiOH in inhibiting alkali-silica reaction at 20 °c: A contribution. Cem Concr Res (2005) 35: 499–504. https://doi.org/10.1016/j.cemconres.2004.06.003.
[50] A. Leemann, L. Bernard, S. Alahrache, F. Winnefeld, ASR prevention - Effect of aluminum and lithium ions on the reaction products. Cem Concr Res (2015) 76: 192-201. https://doi.org/10.1016/j.cemconres.2015.06.002
[51] T. Ramlochan, M. Thomas, K.A. Gruber, Effect of metakaolin on alkali-silica reaction in concrete. Cem Concr Res (2000)30: 339–344. https://doi.org/10.1016/S0008-8846(99)00261-6.
[52] T. Chappex, K. Scrivener, Alkali fixation of C-S-H in blended cement pastes and its relation to alkali silica reaction. Cem Concr Res (2012) 42: 1049–1054. https://doi.org/10.1016/j.cemconres.2012.03.010.
[53] Z. Shi, B. Lothenbach, The role of calcium on the formation of alkali-silica reaction products. Cem Concr Res (2019) 126: 105898. https://doi.org/10.1016/j.cemconres.2019.105898.
[54] E. Boehm-Courjault, S. Barbotin, A. Leemann, K. Scrivener, Microstructure, crystallinity and composition of alkali-silica reaction products in concrete determined by transmission electron microscopy. Cem Concr Res (2020) 130:105988. https://doi.org/10.1016/j.cemconres.2020.105988.
[55] Z. Shi, G. Geng, A. Leemann, B. Lothenbach, Synthesis, characterization, and water uptake property of alkali-silica reaction products. Cem Concr Res (2019) 121: 58–71. https://doi.org/10.1016/j.cemconres.2019.04.009
[56] G. Geng, S. Barbotin, M. Shakoorioskooie, Z. Shi, A. Leemann, D.F. Sanchez, D. Grolimund, E. Wieland, R. Dähn, An in-situ 3D micro-XRD investigation of water uptake by alkali-silica-reaction (ASR) product. Cem Concr Res (2021) 141: 106331. https://doi.org/10.1016/j.cemconres.2020.106331.
[57] Z. Shi, B. Ma, B. Lothenbach, Effect of Al on the formation and structure of alkali-silica reaction products. Cem Concr Res (2021) 140: 106311. https://doi.org/10.1016/j.cemconres.2020.106311.

[58] K.J. Hünger, J. Kronemann, C. Hübert, Y. Scholz, On the mechanism of ASR inhibition by Si and Al containing SCMs. In: 13th Inter Conf Recent Adv Concr Technol Sust Issues, Ottawa, Canada. American Concrete Institute (2015): 437-451.
[59] A. Leemann, Z. Shi, M. Wyrzykowski, F. Winnefeld, Moisture stability of crystalline alkali-silica reaction products formed in concrete exposed to natural environment. Mater Design (2020) 195: 109066. https://doi.org/10.1016/j.matdes.2020.109066.
[60] A. Leemann, Raman microscopy of alkali-silica reaction (ASR) products formed in concrete. Cem Concr Res (2017) 102: 41-47. https://doi.org/10.1016/j.cemconres.2017.08.014.
[61] G. Geng, Z. Shi, A. Leemann, K. Glazyrin, A. Kleppe, D. Daisenberger, S. Churakov, B. Lothenbach, E. Wieland, R. Dähn, Mechanical behavior and phase change of alkali-silica reaction products under hydrostatic compression. Acta Crystallogr B (2020) 76(4). https://doi.org/10.1107/S205252062000846X.
[62] X. Guo, J. Wu, Y.M. Yiu, Y. Hu, Y.J. Zhu, T.K. Sham, Drug–nanocarrier interaction - tracking the local structure of calcium silicate upon ibuprofen loading with X-ray absorption near edge structure (XANES). Phys Chem Chem Phys (2013)15: 15033-15040. https://doi.org/10.1039/C3CP50699A.
[63] G. Geng, Z. Shi, A. Leemann, C. Borca, T. Huthwelker, K. Glazyrin, I.V. Pekov, S. Churakov, B. Lothenbach, R. Dähn, E. Wieland, Atomistic structure of alkali-silica reaction products refined from X-ray diffraction and micro X-ray absorption data. Cem Concr Res (2020) 129: 105958. https://doi.org/10.1016/j.cemconres.2019.105958.
[64] Z. Shi, A. Leemann, D. Rentsch, B. Lothenbach, Synthesis of alkali-silica reaction product structurally identical to that formed in field concrete. Mater Design (2020) 190: 108562. https://doi.org/10.1016/j.matdes.2020.108562.
[65] R. Dähn, A. Arakcheeva, P. Schaub, P. Pattison, G. Chapuis, D. Grolimund, E. Wieland, A. Leemann, Application of micro X-ray diffraction to investigate the reaction products formed by the alkali–silica reaction in concrete structures. Cem Concr Res (2016) 79: 49-56. https://doi.org/10.1016/j.cemconres.2015.07.012.
[66] Z. Shi, B. Lothenbach, The combined effect of potassium, sodium and calcium on the formation of alkali-silica reaction products. Cem Concr Res (2020) 127: 105914. https://doi.org/10.1016/j.cemconres.2019.105914.
[67] N.V. Zubkova, Y.E. Filinchuk, I.V. Pekov, D.Y. Pushcharovsky, E.R. Gobechiya, Crystal structures of shlykovite and cryptophyllite: comparative crystal chemistry of phyllosilicate minerals of the mountainite family. Eur J Mineral (2010) 22(4): 547-555. https://doi.org/10.1127/0935-1221/2010/0022-2041.
[68] Z. Shi, S. Park, B. Lothenbach, A. Leemann, Formation of shlykovite and ASR-P1 in concrete under accelerated alkali-silica reaction at 60 and 80° C. Cem Concr Res (2020) 137: 106213. https://doi.org/10.1016/j.cemconres.2020.106213.
[69] A. Leemann, Z. Shi, J. Lindgård, Characterization of amorphous and crystalline ASR products formed in concrete aggregates. Cem Concr Res (2020) 137: 106190. https://doi.org/10.1016/j.cemconres.2020.106190.
[70] A.J. Maas, J.H. Ideker, M.C. Juenger, Alkali silica reactivity of agglomerated silica fume. Cem Concr Res (2007) 37(2): 166-174. https://doi.org/10.1016/j.cemconres.2006.10.011
[71] G.D. Guthrie, J.W. Carey, A thermodynamic and kinetic model for paste–aggregate interactions and the alkali–silica reaction. Cem Concr Res (2015) 76: 107–120. https://doi.org/10.1016/j.cemconres.2015.05.004.
[72] M. Shakoorioskooie, M. Griffa, A. Leemann, R. Zboray, P. Lura, Alkali-silica reaction products and cracks: X-ray micro-tomography-based analysis of their spatial-temporal evolution at a mesoscale. Cem Concr Res (2021) 150: 106593. https://doi.org/10.1016/j.cemconres.2021.106593.
[73] S. Brisard, M. Serdar, and P. J. M. Monteiro, Multiscale X-ray tomography of cementitious materials: A review. Cem Concr Res (2020) 128: 105824. https://doi.org/10.1016/j.cemconres.2019.105824
[74] O. Stamati, E. Roubin, E. Andò, and Y. Malecot, Phase segmentation of concrete x-ray tomographic images at meso-scale: Validation with neutron tomography. Cem Concr Compos (2018) 88:8-16. https://doi.org/10.1016/j.cemconcomp.2017.12.011
[75] T. Knudsen, N. Thaulow, Quantitative microanalyses of alkali-silica gel in concrete, Cem Concr Res (1975) 5(5): 443–454, https://doi.org/10.1016/0008-8846(75)90019-8.
[76] V. Jensen, Alkali-aggregate reaction in Southern Norway. Doctoral Thesis, Technical University of Trondheim, NTH, Norway, 1993.
[77] D. Hernández-Cruz, C.W. Hargis, J. Dominowski, M.J. Radler, P.J.M. Monteiro, Fiber reinforced mortar affected by alkali-silica reaction: A study by synchrotron microtomography. Cem Concr Compos (2016) 68: 123–130. https://doi.org/10.1016/j.cemconcomp.2016.02.003.
[78] A.D. Jensen, S. Chatterji, P. Christensen, N. Thaulow, Studies of alkali-silica reaction - part II effect of air-entrainment on expansion. Cem Concr Res (1984) 14(3): 311–314. https://doi.org/10.1016/0008-8846(84)90046-2.
[79] E.R. Gallyamov, R. Rezakhani, M. Corrado, J.-F. Molinari, Meso-scale modelling of ASR in concrete: effect of viscoelasticity. Proc 16th ICAAR, Volume I, Lisbon/Portugal, 2021.
[80] R. Rezakhani, E.R. Gallyamov, J.-F. Molinari, Meso-scale finite element modeling of alkali-silica-reaction. Constr Build Mater (2021) 278: 122244. https://doi.org/10.1016/j.conbuildmat.2021.122244.
[81] E.R. Gallyamov, A.I. Cuba Ramos, M. Corrado, R. Rezakhani, J.-F. Molinari, Multi-scale modelling of concrete structures affected by alkali-silica reaction: Coupling the mesoscopic damage evolution and the macroscopic concrete deterioration. Int J Solids Struct (2020) 207: 262-278. https://doi.org/10.1016/j.ijsolstr.2020.10.010.
[82] E.R. Gallyamov, A. Leemann, B. Lothenbach. J.-F. Molinari, Predicting damage in aggregates due to the volume increase of the alkali-silica reaction products. Cem Concr Res (2022) 154: 106744. https://doi.org/10.1016/j.cemconres.2022.106744
[83] N. Richart, J. Molinari, Implementation of a parallel finite-element library: Test case on a non-local continuum damage model. Finite Elem Anal Des (2015) 100: 41–46. https://doi.org/10.1016/j.finel.2015.02.003.
[84] T. Oey, E. C. La Plante, G. Falzone, Y. H. Hsiao, A. Wada, L. Monfardini, M. Bauchy, J.W. Bullard, G. Sant, Calcium nitrate: A chemical admixture to inhibit aggregate dissolution and mitigate expansion caused by alkali-silica reaction. Cem Concr Compos (2020) 110: 103592. https://doi.org/10.1016/j.cemconcomp.2020.103592.
[85] G. Kaladharan, T. Szeles, S.M. Stoffels, F. Rajabipour, Novel admixtures for mitigation of alkali-silica reaction in concrete. Cem Concr Compos (2021) 120: 104028. https://doi.org/10.1016/j.cemconcomp.2021.104028.
[86] J. Zhou, K. Zheng, Z. Liu, L. Chen, N. Lippiatt, Use of γ-Al_2O_3 to prevent alkali-silica reaction by altering solid and aqueous compositions of hydrated cement paste. Cem Concr Res (2019) 124: 105817. https://doi.org/10.1016/j.cemconres.2019.105817.